Journal Pre-proof

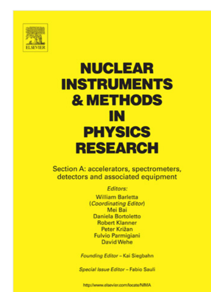

Mo/4H-SiC Schottky diodes for room temperature X-ray and γ-ray spectroscopy

G. Lioliou, A.B. Renz, V.A. Shah, P.M. Gammon, A.M. Barnett

PII: S0168-9002(22)00020-1
DOI: https://doi.org/10.1016/j.nima.2022.166330
Reference: NIMA 166330

To appear in: *Nuclear Inst. and Methods in Physics Research, A*

Received date : 9 June 2021
Revised date : 21 December 2021
Accepted date : 3 January 2022

Please cite this article as: G. Lioliou, A.B. Renz, V.A. Shah et al., Mo/4H-SiC Schottky diodes for room temperature X-ray and γ-ray spectroscopy, *Nuclear Inst. and Methods in Physics Research, A* (2022), doi: https://doi.org/10.1016/j.nima.2022.166330.

This is a PDF file of an article that has undergone enhancements after acceptance, such as the addition of a cover page and metadata, and formatting for readability, but it is not yet the definitive version of record. This version will undergo additional copyediting, typesetting and review before it is published in its final form, but we are providing this version to give early visibility of the article. Please note that, during the production process, errors may be discovered which could affect the content, and all legal disclaimers that apply to the journal pertain.

© 2022 Elsevier B.V. All rights reserved.

Journal Pre-proof

1 **Mo/4H-SiC Schottky diodes for room temperature X-ray and γ-ray spectroscopy**

2 G. Lioliou[1*], A.B. Renz[2], V.A. Shah[2], P.M. Gammon[2], and A.M. Barnett[1]
3
4 [1]*Space Research Group, Sch. of Mathematical and Physical Sciences, University of Sussex, Falmer,*
5 *Brighton, BN1 9QT, UK*
6 [2]*School of Engineering, University of Warwick, Coventry, CV4 7AL, UK*
7

8 **ABSTRACT.** Mo/4H-SiC Schottky diodes were investigated as detectors for their suitability
9 in photon counting X-ray and γ-ray spectroscopy. The Schottky diodes, with a 35 μm thick
10 n^- epitaxial layer, were treated with a phosphorus pentoxide surface passivation, which had
11 been previously shown to improve the homogeneity of the metal-semiconductor interface and
12 supress leakage current. One device was coupled to a low-noise charge sensitive preamplifier
13 and standard onwards readout electronics; the resultant spectrometer was used to
14 accumulated X-ray and γ-ray spectra. The spectrometer had an energy resolution of 1.67 keV
15 ± 0.08 keV (97 e^- rms ± 5 e^- rms) at 5.9 keV and 1.6 keV ± 0.1 keV (93 e^- rms ± 6 e^- rms) at
16 59.54 keV. Despite the moderate energy resolution achieved, the results suggested that the
17 leakage current of the Mo/4H-SiC Schottky diode detector was not the dominant source of
18 noise limiting the energy resolution of the spectrometer at the optimum operating conditions
19 at room temperature; lossy dielectrics in close proximity to the input of the preamplifier
20 (including stray dielectrics) and the relatively large average electron-hole pair creation energy
21 of 4H-SiC (an inherent property) were the main contributors to the achieved energy
22 resolution in energy terms.
23

24 Keywords: 4H-SiC; Schottky diodes; Mo Schottky contact; X-ray spectroscopy; γ-ray
25 spectroscopy.
26

27 1. Introduction

28 4H-SiC is one of the most mature wide bandgap semiconductor materials. The advantages of
29 this SiC polytype over Si have led to the development of high performing 4H-SiC detectors
30 for X-ray and γ-ray spectroscopy, particularly for harsh environments where instrumentation
31 is required to operate at high temperature or when exposed to intense radiation.
32

33 Uncooled operation of semiconductor radiation detectors at high temperatures (≥ 20 °C)
34 requires a wide bandgap. The bandgap of 4H-SiC, 3.2 eV [1], is almost three times wider
35 than that of Si, resulting in low thermally generating leakage currents. Indeed, 4H-SiC based
36 radiation detectors have been reported with leakage current densities as low as 0.1 pA cm^{-2} at
37 25 °C, while typical Si radiation detectors have leakage currents four orders of magnitude
38 higher (~ 1 nA cm^{-2}) [2]. Another advantage of 4H-SiC is its relatively low electron affinity
39 (3.17 eV [3]). This allows Schottky diodes with high barrier height to be fabricated, reducing
40 the thermionic emission current component. These intrinsic characteristics minimise the
41 parallel white noise originating from the 4H-SiC radiation detector, which contribute to the
42 total noise of the photon counting spectroscopic system. Additionally, a 4H-SiC detector

[*] Corresponding author. Tel.: +44 (0) 1273 872568. E-mail address: G.Lioliou@sussex.ac.uk

Journal Pre-proof

Journal Pre-proof

43 based X-ray and γ-ray spectrometer may also benefit from little or no incomplete charge
44 collection noise by virtue of the high quality material available, and considering the relatively
45 high electric field strengths that can be applied to the detector due to the material's high
46 breakdown field (3×10^6 V cm^{-1} to 5×10^6 V cm^{-1} at 300 K [4]). The high tolerance of 4H-
47 SiC to radiation damage, a useful attribute of radiation detectors operating in intense radiation
48 environments (such as certain space environments, civil nuclear applications, and some
49 nuclear defence situations), further motivates the development and deployment of such
50 detectors. 4H-SiC radiation detectors have been found to be more radiation hard than Si
51 detectors [5-7], increasing the life-time of the respective spectrometer, while being subjected
52 to intense radiation.
53
54 The development of 4H-SiC detector based X-ray and γ-ray spectrometers started by utilizing
55 Au/4H-SiC Schottky diodes; initially, an energy resolution (Full Width at Half Maximum,
56 FWHM) poorer than 2.7 keV at 59.54 keV at room temperature was reported [8]. Progress in
57 4H-SiC epitaxial growth and in ultra-low noise preamplifier electronics resulted in the
58 advancement of single pixel spectroscopic systems employing Au/4H-SiC Schottky diodes
59 over the decade which followed, with an energy resolution of 196 eV FWHM at 5.9 keV at
60 30 °C being reported some ten years later [9]. NiSi/4H-SiC Schottky diodes, in an array
61 configuration, have also been investigated for their suitability in X-ray photon counting
62 spectroscopy [10-12]. The best energy resolution achieved with NiSi/4H-SiC Schottky
63 diodes was 1.36 keV FWHM at 17.4 keV, at 30 °C, which was limited by the stray
64 capacitances and dielectrics at the input of the preamplifier, rather than the detector itself
65 [12]. Ni_2Si/4H-SiC Schottky diodes were shown to be suitable for X-ray photon counting
66 spectroscopy, up to 100 °C, with an energy resolution of 1.26 keV FWHM at 5.9 keV at 20
67 °C; the noise of the spectrometer was greatly limited by stray dielectrics [13]. Commercial-
68 off-the-shelf 4H-SiC UV p-n photodiodes, have been repurposed as detectors for photon
69 counting X-ray and γ-ray spectroscopy [14-15]. The energy resolution of that spectrometer
70 operating at 20 °C varied from 1.66 keV ± 0.15 keV at 5.9 keV to 1.83 keV ± 0.15 keV at
71 59.5 keV [15].
72
73 The relatively high average electron-hole pair creation energy of 4H-SiC (7.8 eV [9]) places
74 greater demands (cf. detector materials with smaller electron-hole pair creation energies,
75 including Si, GaAs, $In_{0.5}Ga_{0.5}P$, and $Al_{0.52}In_{0.48}P$) on the charge sensitive preamplifier
76 employed in a radiation spectrometer. When both spectrometers have identical equivalent
77 noise charge (ENC, in units of e^- rms), the energy resolution (FWHM) achieved with a 4H-
78 SiC detector based spectrometer is poorer than that achieved with a spectrometer employing a
79 detector which has a smaller electron-hole pair creation energy, due to the larger average
80 electron-hole pair creation energy of 4H-SiC. However, the advantage from using a wider
81 bandgap detector, such as one made from 4H-SiC, compared to a detector with a narrower
82 bandgap, comes at high temperatures where the ENC contribution of the narrower bandgap
83 detector can be greater than that of the wider bandgap detector by a sufficient amount as to
84 outweigh the larger average electron-hole pair creation energy of the wider bandgap detector.
85

Journal Pre-proof

86 The work function of the metal of the Schottky contact on a 4H-SiC Schottky diode defines
87 the Schottky barrier height of the diode: in the ideal case, the Schottky barrier height equals
88 the difference between the metal work function and the electron affinity of the semiconductor
89 [16]. Achieving high barrier heights, and thus supressed thermionic emission currents,
90 requires the use of a metal with high work function; work functions of 5.1 eV for Au [17], 4.8
91 eV for Ni_2Si, and 4.5 eV for NiSi [18] have been reported. Recently, another metal, Mo, has
92 been considered for the Schottky contact on 4H-SiC Schottky diodes. Although the work
93 function of Mo is relatively low, between 4.36 eV and 4.95 eV, depending on its
94 crystallographic orientation [19], promising results have been reported concerning
95 overcoming the disadvantage (higher leakage currents) of the relatively low barrier heights of
96 Mo/4H-SiC Schottky diodes [20]. Surface passivation treatments using phosphorus
97 pentoxide (P_2O_5) prior to the metal deposition have been shown to homogenize the Mo/4H-
98 SiC interface, increase the resulting Schottky barrier height, and reduce leakage currents by
99 up to three orders of magnitude cf. untreated Mo/4H-SiC Schottky diodes [21-22].
100
101 Here, Mo/4H-SiC Schottky diodes treated by a P_2O_5 surface passivation are investigated for
102 their suitability in X-ray and γ-ray photon counting spectroscopy for the first time. A total of
103 six diodes were studied. Initially, the dark current and the capacitance of each diode was
104 measured at room temperature (≈ 20 °C); one representative device was then characterised at
105 temperatures, T, -40 °C $\leq T \leq$ 140 °C. In all cases, the important parameters (saturation
106 current, barrier height, ideality factor, leakage current density, depletion layer width, effective
107 carrier concentration) of the Schottky didoes were calculated. One randomly selected device
108 was then coupled, as a radiation detector, to a low-noise charge sensitive preamplifier and
109 regular onwards nuclear electronics readout instrumentation to realise a photon counting
110 radiation spectrometer; subsequently, X-ray and γ-ray spectra were accumulated. The
111 spectrometer was operated at room temperature and the detector was directly illuminated by
112 photons from three radioisotope radiation sources, which provided photons with energies ≤
113 88.04 keV. Shaping time noise analysis of the X-ray and γ-ray spectra accumulated with the
114 Mo/4H-SiC Schottky diode based spectrometer allowed the identification of the main factors
115 limiting its energy resolution.
116

117 **2. Methods**

118 *2. 1. Device structure and fabrication procedure*

119 Mo/SiC Schottky diodes were fabricated using n^+ type (nitrogen-doped), 4° off-axis, 4H-SiC
120 substrates, on which an n^- type (1×10^{15} cm^{-3}) 35 μm thick epitaxial layer was grown. The
121 resultant wafer was diced into chips; they were cleaned using a standard
122 RCA1/HF(10%)/RCA2/HF(10%) process. The surface passivation routine followed: the
123 samples were mounted on a carrier wafer and placed in front of a silicon diphosphate
124 (SiP_2O_7) source wafer; P_2O_5 was deposited (in a tube furnace at 1000 °C) for 2 hours. The
125 wafers were cleaned in dilute HF (10%) to remove the oxide layers. A 1 μm thick SiO_2 layer
126 was deposited, for insulation, by Low Pressure Chemical Vapor Deposition (LPCVD) using
127 tetraethyl orthosilicate (TEOS) while a Si precursor covered the active areas before contact
128 formation. Ti/Ni (30 nm/100 nm) ohmic contacts were formed on the rear of the samples
129 after a rapid thermal anneal at 1000 °C for 2 minutes in Ar (5 slm) ambient. The Schottky

Journal Pre-proof

130 contacts were then formed by opening a window in the thick SiO_2 layer and evaporating
131 100 nm of Mo before annealing at 500 °C in Ar (5 slm) ambient. Finally, a 1 µm thick Al
132 metal overlay, serving as a field plate, was evaporated on top of the die. A total of six
133 devices, D1 – D6, on a single die were studied; the six diodes were randomly selected from
134 those fabricated. Each device was a stadium shape, which had dimensions of 350 µm
135 (length) by 136 µm (width) and an area (considering the rounded corners) of 0.0439 mm^2.
136 The gap between adjacent devices was 129 µm and 156 µm in the length and width
137 dimensions, respectively. The devices were packaged (mounted using silver-loaded epoxy in
138 a TO-5 can, and ball-wedge wirebonded) to ease handling. A schematic diagram showing the
139 identification numbers of the six devices and their relative locations, is shown in **Figure 1**.
140

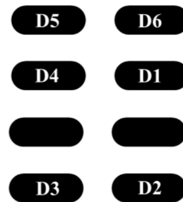

141
142 Figure 1. Schematic diagram showing the investigated six devices on the die along with their
143 identification numbers.
144
145 Calculations of the devices' X-ray/γ-ray quantum detection efficiency are presented in
146 Section *3. 1. Quantum detection efficiency*.
147
148 *2. 2. Current and capacitance measurements*
149 The dark currents and the capacitances of each of the six Mo/4H-SiC Schottky diodes, D1 –
150 D6, were measured at room temperature, the characteristics of one representative device, D3,
151 were also measured at temperatures T, -40 °C $\leq T \leq$ 140 °C. Since every device was
152 packaged in a TO-5 can, accompanying measurements (dark current and capacitance) were
153 also performed of the package alone; the contribution of the package to the dark current and
154 the capacitance was thus separated and the results presented below correspond to the
155 contribution of each diode itself (i.e. with the packaging contributions subtracted), except
156 where indicated.
157
158 For characterisation, the devices were installed in an optically-dark and electromagnetically-
159 shielded Al test enclosure. The enclosure was kept at ≈ 20 °C for the room temperature
160 measurements of all six diodes. For the temperature dependent characterisation of the
161 selected diode, the enclosure was placed in a Temperature Applied Science Ltd Micro LT
162 climatic cabinet which was used to achieve temperatures across the investigated range, in 20
163 °C steps. Any unwanted, humidity-related, effects were eliminated by continually purging
164 with dry N_2 (relative humidity ≤ 5%): for the room temperature measurements, the enclosure
165 was purged directly and continuously; for the temperature dependent measurements, the
166 enclosure was initially purged directly, then the climatic cabinet was purged directly and
167 continuously with the enclosure within it.

Journal Pre-proof

Journal Pre-proof

168
169 The measurements of the dark currents as function of applied bias were performed using a
170 Keithley 6487 Picoammeter/Voltage Source. The bias applied during the dark current
171 measurements ranged from 0 V to 200 V in the reverse polarity, in 1 V steps, and from 0 V to
172 0.9 V in the forward polarity, in 0.05 V steps. The measurements of capacitance as a
173 function of applied bias were performed using an HP 4275A Multi Frequency LCR meter
174 employing a test signal (50 mV rms magnitude; 1 MHz frequency); the biases (from 0 V to
175 200 V reverse bias, in 1 V steps) for the capacitance measurements were applied using a
176 Keithley 6487 Picoammeter/Voltage Source.
177
178 The measurements and their interpretation are presented in Section *3. 2. Current*
179 *measurements*.
180
181 *2. 3. X-ray and γ-ray spectroscopy*
182 One randomly selected diode, D2, was then investigated for its X-ray and γ-ray photon
183 counting spectroscopic performance at room temperature (≈ 20 °C). X-ray and γ-ray spectra
184 of three radioisotope radiation sources (an ^{55}Fe radioisotope X-ray source, a ^{109}Cd
185 radioisotope X-ray and γ-ray source, and an ^{241}Am radioisotope X-ray and γ-ray source) were
186 accumulated and the performance of the spectrometer was studied.
187
188 The spectrometer comprised the radiation detector, a charge sensitive preamplifier (CSP), a
189 shaping amplifier (SA), and a multi-channel analyser (MCA) which was connected to a
190 personal computer. The detector was coupled to the input of the CSP. Instead of using
191 commercially available preamplifier electronics for X-ray and γ-ray spectroscopy, a custom-
192 made CSP with a lower noise level was employed. The CSP operated with its input
193 transistor, an NJ26 JFET, slightly forward biased. This configuration of the CSP eliminated
194 the feedback resistor and external reset circuity typically found in many CSP designs; it thus
195 resulted in improved noise performance [23]. The pulse amplification and shaping of the
196 output of the CSP was achieved with an ORTEC 572A SA; it had a semi-Gaussian pulse
197 shape with a selectable shaping time (0.5 μs, 1 μs, 2 μs, 3 μs, 6 μs, and 10 μs). The output of
198 the SA was then connected to an ORTEC EASYMCA 8k MCA, which performed the
199 digitalization of the pulses. Similar to the dark current and capacitance measurements, the
200 detector was again operated in a dry N_2 environment to eliminate any possible humidity-
201 related effects. The detector was reverse biased using a Keithley 6487 Picoammeter/Voltage
202 Source.
203
204 Initially, the detector was illuminated by photons from the ^{55}Fe radioisotope X-ray source.
205 ^{55}Fe radioisotope X-ray spectra were accumulated with the detector operated at 50 V, 100 V,
206 and 150 V applied reverse bias and at all available shaping times. Studying the performance
207 of the spectrometer as a function of detector applied reverse bias and shaping time allowed a
208 better understanding of the different noise contributions to its energy resolution, it also
209 allowed identification of the optimum operating conditions (i.e. those which gave the best
210 energy resolution). Following this, one ^{109}Cd radioisotope X-ray and γ-ray spectrum and one
211 ^{241}Am radioisotope X-ray and γ-ray spectrum were obtained at the optimum available shaping

212 time and applied reverse bias, to investigate the performance of the spectrometer at higher
213 photon energies. The live time limit of the spectra were 180 s for each ^{55}Fe radioisotope X-
214 ray spectrum, and 43200 s for each of the ^{109}Cd and ^{241}Am radioisotope X-ray and γ-ray
215 spectra. Prior preparatory investigation had shown that the systems used were stable over
216 such durations.
217
218 The ^{55}Fe radioisotope X-ray source, which had an activity of 93 MBq, emitted characteristic
219 Mn Kα (5.9 keV) and Mn Kβ (6.49 keV) X-rays; the relative emission ratio between the Mn
220 Kβ and Mn Kα lines was 0.138 [24]. The ^{109}Cd radioisotope X-ray and γ-ray source, which
221 had an activity of 168 MBq, emitted characteristic Ag $K\alpha_1$ (22.16 keV), $K\alpha_2$ (21.99 keV), Kβ
222 (24.9 keV), Lα (2.98 keV) X-rays, and 88.03 keV γ-rays [25]. The emission ratio between
223 the Ag Kα and the Ag Kβ was 5.54. The ^{241}Am X-ray and γ-ray radioisotope source, which
224 had an activity of 299 MBq, emitted characteristic Np Lα (13.76 keV and 13.95 keV), Lβ
225 (ranging from 16.11 keV to 17.99 keV), and Lγ (ranging from 20.78 keV to 21.49 keV) X-
226 rays [26], and 26.3 keV, 33.2 keV, 43.4 keV, and 59.54 keV γ-rays [27]. Each radioisotope
227 radiation source was individually encapsulated in a stainless steel housing with a 250 μm
228 thick Be X-ray/γ-ray window.
229
230 The spectra and their interpretation are presented in Section *3. 4. X-ray and γ-ray*
231 *spectroscopy measurements*.
232
233 **3. Results**
234 *3. 1. Quantum detection efficiency*
235 The quantum detection efficiency, *QE*, of the Mo/4H-SiC Schottky diode detectors was
236 calculated for photon energies within the range 1 keV to 100 keV. The quantum detection
237 efficiency depends upon the attenuation of photons prior to reaching the active region of the
238 detector as well as the absorption of photons within the active region. The active region can
239 be approximated to the depletion region, a region in which, upon the application of an electric
240 field, the photogenerated charge carriers are swept towards the respective electrodes; the
241 movement of the charge carriers results in the production of the signal from the radiation
242 detection [28-29]. As such, when designing radiation detectors, it is typically preferable that
243 the attenuation of photons within the front dead layers be reduced whilst seeking to increase
244 the absorption of photons within the active region. For the present devices, the quantum
245 detection efficiency was calculated using the Beer-Lambert law [30]. The linear attenuation
246 and absorption coefficients, each as functions of photon energy, of the materials comprising
247 the detectors' structure (Al, Mo, and 4H-SiC) were extracted from Hubbell and Seltzer [31].
248 The 1 μm thick Al layer and the 100 nm thick Mo Schottky contact were considered to be
249 inactive (dead layers) whereas the depleted part of the n^- epitaxial layer was considered to be
250 active. The results of the *QE* calculations can be seen in **Figure 2**. Two cases were
251 considered: the *QE* for a fully depleted n^- epitaxial layer (35 μm) and the *QE* achieved under
252 the application of 150 V reverse bias (4.6 μm ± 0.6 μm) (see Section *3. 3. Capacitance*
253 *measurements*). Based on the effective carrier concentration within the n^- epitaxial layer as
254 determined from the capacitance measurements, full depletion of the epitaxial layer would
255 have required an applied reverse bias of 8000 V.

Journal Pre-proof

Journal Pre-proof

256

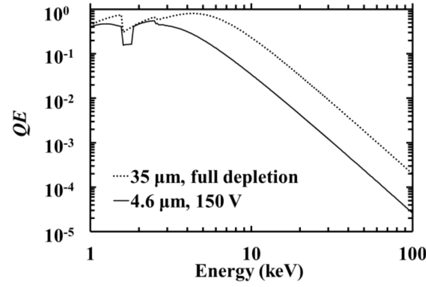

257
258 Figure 2. Quantum detection efficiency, *QE*, as functions of photon energy for the detector if
259 it was fully depleted (···) and when it was reverse biased at 150 V (—).
260
261 As is characteristic for thin radiation detectors made from materials with relatively low linear
262 attenuation coefficients, the *QE* reduced significantly as the photon energy increased; *QE* of
263 0.6638 at 5.9 keV, 0.0235 at 22.16 keV, 0.0010 at 59.54 keV, and 0.0003 at 88.03 keV were
264 calculated for the notional case in which the n^- epitaxial layer was fully depleted. However,
265 for the 150 V bias condition, in which the detector was operated, the *QE* values at the same
266 energies were 0.1406, 0.0031, 0.00014, and 0.00004. Whilst 4H-SiC is a wide bandgap
267 material, and it can thus operate at higher temperatures than Si detectors, the linear
268 attenuation coefficients of 4H-SiC are near identical to those of Si. Si detectors are available
269 with much thicker active regions than those of any 4H-SiC detector so far reported, as such Si
270 detectors commonly have higher *QE* than 4H-SiC detectors. Many other wide bandgap
271 semiconductors (e.g. GaAs, $In_{0.5}Ga_{0.5}P$, and $Al_{0.52}In_{0.48}P$) have far better linear attenuation
272 coefficients than 4H-SiC and Si, and hence can achieve the same or better *QE* values with
273 thinner epitaxial layers.
274
275 The abrupt discontinuities in present in the *QE* as shown in **Figure 2** are at the characteristic
276 absorption edges, which occurring at energies equal to the binding energies of the atoms
277 within the detector; absorption edges at ≈ 1.5 keV (Al K edge), at ≈ 1.7 keV (Si K edge), and
278 at ≈ 2.4 keV (Mo L edge).
279
280 *3. 2. Current measurements*
281 The dark currents of the six Mo/4H-SiC Schottky diodes at room temperature, under reverse
282 and forward applied bias, are presented in **Figure 3**. The leakage currents (dark current
283 under applied reverse bias, **Figure 3 (a)**) of D1 – D6 were the same, within uncertainties, at
284 applied reverse bias ≤ 140 V. The mean leakage current across all devices was 1.8×10^{-12} A
285 $\pm 0.3 \times 10^{-12}$ A (rms deviance) at 140 V applied reverse bias, at room temperature. However,
286 the leakage current at > 140 V applied reverse bias differed among different devices. It
287 ranged between 31.9×10^{-12} A $\pm 0.5 \times 10^{-12}$ A for D4 (the minimum) and 139.9×10^{-12} A ±
288 0.8×10^{-12} A for D6 (the maximum) at 200 V applied reverse bias. Although the shape of the
289 forward current as a function of applied forward bias (**Figure 3 (b)**) was the same for all
290 devices, the values of forward current at high applied forward biases differed between
291 different devices. For example, it ranged from 0.802×10^{-3} A $\pm 0.001 \times 10^{-3}$ A for D5 (the

Journal Pre-proof

292 minimum) to 2.391 × 10^{-3} A ± 0.003 × 10^{-3} A for D2 (the maximum) at 0.9 V applied
293 forward bias. The observed differences in the measured currents (at room temperature) of the
294 devices were attributed to potential slight inhomogeneities from device to device.
295

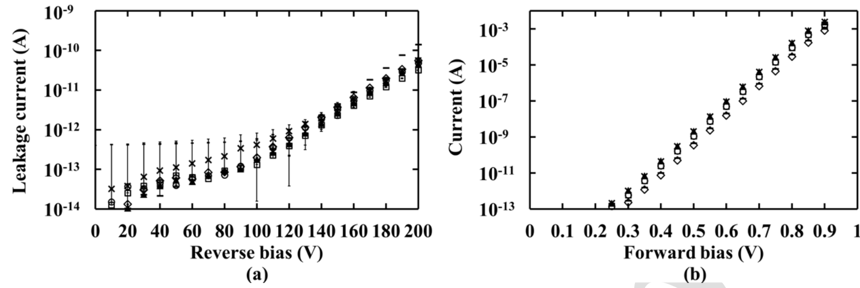

296
297 Figure 3. Dark current as a function of applied (a) reverse (in 10 V steps to improve clarity)
298 and (b) forward bias at room temperature, of the six Mo/4H-SiC Schottky diodes: D1 (○); D2
299 (▲); D3 (×); D4 (□); D5 (◇); D6 (—). The error bars were smaller than the symbol sizes in
300 (b).
301
302 Assuming that the leakage current of the devices originated in the bulk, the leakage current
303 density was calculated by dividing the leakage current (**Figure 3 (a)**) by the total area. The
304 calculated leakage current densities at applied reverse biases of: 100 V (corresponding to an
305 applied electric field strength of ≈ 265 kV cm^{-1}); 150 V (corresponding to an applied electric
306 field strength of ≈ 330 kV cm^{-1}); and 200 V (corresponding to an applied electric field
307 strength of ≈ 370 kV cm^{-1}), can be seen in **Figure 4**. At 100 V, the leakage current density
308 was found to be the same for all devices; its mean value was 5 × 10^{-10} A cm^{-2} ± 2 × 10^{-10} A
309 cm^{-2} (rms deviance). However, at 150 V and 200 V, the leakage current density differed
310 between devices. At 150 V, the leakage current density ranged from 5.3 × 10^{-9} A cm^{-2} ± 0.9
311 × 10^{-9} A cm^{-2} for D4 (the minimum) and 10.0 × 10^{-9} A cm^{-2} ± 0.9 × 10^{-9} A cm^{-2} for D6 (the
312 maximum). At 200 V, the leakage current density ranged from 0.73 × 10^{-7} A cm^{-2} ± 0.01 ×
313 10^{-7} A cm^{-2} for D4 (again, the minimum) and 3.19 × 10^{-7} A cm^{-2} ± 0.02 × 10^{-7} A cm^{-2} for D6
314 (again, the maximum). It should be noted that such applied electric field strengths were
315 extremely high for a semiconductor radiation detector [9].
316
317 At room temperature, the leakage current density of all six Mo/4H-SiC Schottky diodes when
318 operated at an applied electric field strength of 103 kV cm^{-1} (the field strength at which other
319 high quality 4H-SiC devices have been reported previously) was below the noise floor of the
320 measurement system and thus ≤ 84 × 10^{-12} A cm^{-2}, given the performance of the
321 instrumentation and the geometry of the detectors. The ultra-low leakage currents measured
322 for the Mo/4H-SiC Schottky diodes were in part attributed to the P_2O_5 surface passivation
323 [21-22].
324
325 Ultra-high quality 4H-SiC Schottky diodes of 70 µm epitaxial layer thickness and with
326 circular Au Schottky contacts (200 µm in diameter) have been reported with leakage current
327 densities ~ 10^{-12} A cm^{-2} at room temperature and the same applied electric field strength as

Journal Pre-proof

328 above [9]. It is with those devices, and exceptionally low noise CSP electronics, that the best
329 energy resolutions so far achieved with 4H-SiC radiation detectors have been reported.
330

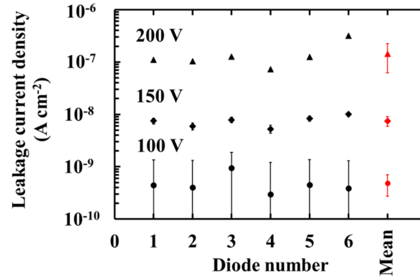

331
332 Figure 4. Leakage current density at room temperature for the six Mo/4H-SiC Schottky
333 diodes at: 100 V applied reverse bias (corresponding to an applied electric field strength of ≈
334 265 kV cm^{-1}) (●); 150 V applied reverse bias (corresponding to an applied electric field
335 strength of ≈ 330 kV cm^{-1}) (◆); and 200 V applied reverse bias (corresponding to an applied
336 electric field strength of ≈ 370 kV cm^{-1}) (▲). At each reverse bias, the mean value and the
337 associated rms deviance is also shown.
338

339 The saturation current, barrier height, and ideality factor were then calculated for each of the
340 six Mo/4H-SiC Schottky diodes at room temperature. Current transport in the Schottky
341 diodes was assumed to be governed by thermionic emission and diffusion (i.e.
342 recombination-generation current was assumed to be negligible). Thus, generalized
343 thermionic-emission-diffusion theory [16] was used to describe the forward current in the
344 Schottky diodes and to extract the corresponding parameters. Initially, the saturation current
345 was calculated from the extrapolation of the linear region of the dark current as a function of
346 forward bias (**Figure 3 (b)**) to the point of its interception with the current axis. The results
347 can be seen in **Figure 5**. The saturation current ranged from 1.22×10^{-18} A ± 0.05×10^{-18} A
348 for D5 (the minimum) to 9×10^{-18} A ± 1×10^{-18} A for D2 and D3 (the maxima). The mean
349 saturation current (across all devices) at room temperature was 5×10^{-18} A ± 3×10^{-18} A (rms
350 deviance).
351

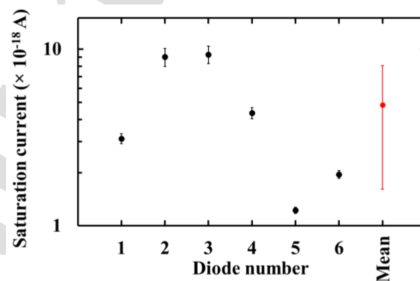

352
353 Figure 5. Saturation current of the six Mo/4H-SiC Schottky diodes at room temperature. The
354 mean and rms deviance is also shown.
355

Journal Pre-proof

356 The calculated saturation current of each device was then used to calculate the zero band
357 barrier height since the latter is a function of only the saturation current and the area of the
358 Schottky diode at any given temperature [16]. The barrier heights of D1 – D6 are presented
359 in **Figure 6**. All the diodes had the same barrier height at room temperature; a mean value of
360 1.23 eV ± 0.02 eV (rms deviance) was calculated. The experimental uncertainties associated
361 with the measurements were greater than the rms uncertainty, as such it would be more correct to
362 consider the mean barrier height to have an uncertainty which is better quantified by the
363 experimental uncertainty of the mean (combining all individual experimental uncertainties),
364 i.e. ± 0.03 eV. However, even considering the smaller rms uncertainty, the calculated barrier
365 height was the same, within uncertainties, as the barrier height measured for previously
366 reported Mo/4H-SiC Schottky diodes (which had also undergone a P_2O_5 surface passivation
367 treatment), i.e. 1.27 eV ± 0.032 eV (standard deviation) [22]. The barrier height, ideally,
368 equals the difference between the electron affinity of the semiconductor and the metal work
369 function [16]. The electron affinity of 4H-SiC is 3.17 eV [3] and the work function of Mo is
370 4.36 eV – 4.95 eV depending on its crystallographic orientation [19]. Thus, the calculated
371 mean barrier height of the Mo/4H-SiC Schottky diodes was as had been expected.
372

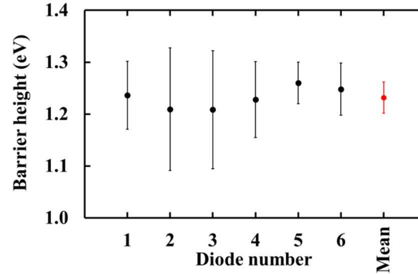

373
374 Figure 6. Barrier height of the six Mo/4H-SiC Schottky diodes at room temperature. The
375 mean and rms deviance is also shown.
376

377 The ideality factor was then extracted from the measurements of dark current as a function of
378 forward bias [16]. First, the derivative of the applied forward bias, V_{AF}, with respect to the
379 forward current, I_F, $\frac{d(V_{AF})}{d(lnI_F)}$, was plotted as a function of the forward current, I_F. Then, the
380 linear region of this plot was identified quantitatively by linear least squares fitting; the
381 intercept point of the line of best fit to the $\frac{d(V_{AF})}{d(lnI_F)}$ axis was used to calculate the ideality factor.
382 The ideality factor of each device is plotted in **Figure 7**. The mean ideality factor (across all
383 devices) was 1.01 ± 0.01 (rms deviance). The experimental uncertainties associated with the
384 ideality factor measurements (± 0.02) were greater than the rms uncertainty; the experimental
385 uncertainty of the mean (combining all individual experimental uncertainties) was calculated
386 to be ± 0.01. Two observations were made from the calculated ideality factor values. Firstly,
387 the assumption that the current transport mechanism was governed by thermionic emission
388 and diffusion, was supported by the demined ideality factors, given that they were = 1.
389 Secondly, the presently reported devices had the same ideality factor, within uncertainties, as

Journal Pre-proof

Journal Pre-proof

previously reported Mo/4H-SiC Schottky diodes which had also undergone a P_2O_5 surface passivation treatment (ideality factors of 1.02 eV ± 0.005 eV [22]).

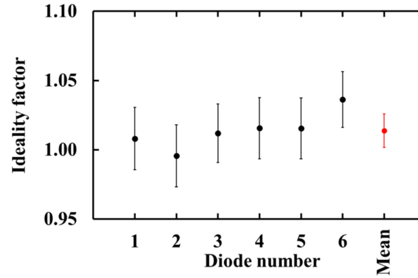

Figure 7. Ideality factor of the six Mo/4H-SiC Schottky diodes at room temperature. The mean and rms deviance is also shown.

One representative diode, D3, was then selected which had neither the highest nor the lowest current (**Figure 3** and **Figure 4**); its current-related applied reverse bias characteristics were then further investigated as functions of temperature. **Figure 8** shows the detector's dark current as functions of applied reverse and forward bias across the temperature range 140 °C ≤ T ≤ -40 °C. Both the reverse (leakage) and forward current reduced as the temperature was decreased from 140 °C to -40 °C. As an example, at 150 V, the leakage current decreased from 6.21×10^{-10} A ± 0.02×10^{-10} A at 140 °C to 0.3×10^{-12} A ± 0.4×10^{-12} A at -40 °C.

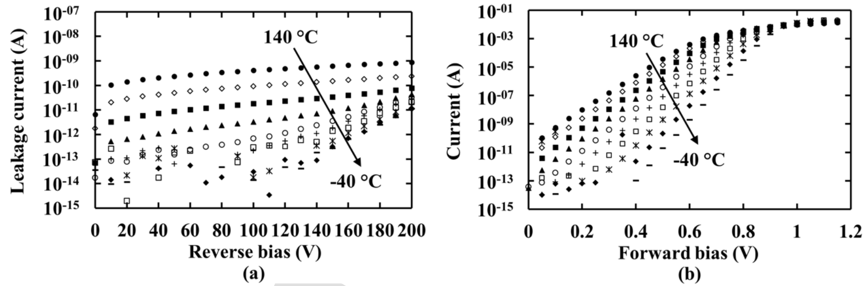

Figure 8. (a) Reverse and (b) forward current as a function of applied reverse bias at temperatures, T, 140 °C ≤ T ≤ -40 °C, for diode D3. The error bars have been omitted for clarity.

Similarly to the calculations of leakage current density at room temperature (**Figure 4**), the leakage current density of D3 was calculated as a function of temperature. The leakage current density at two selected applied reverse biases (150 V, corresponding to an applied electric field strength of ≈ 330 kV cm^{-1}; and 200 V, corresponding to an applied electric field strength of ≈ 370 kV cm^{-1}) can be seen in **Figure 9** as functions of temperature. At 150 V, the leakage current reduced from 1.415×10^{-6} A cm^{-2} ± 0.005×10^{-6} A cm^{-2} at 140 °C to 6×10^{-10} A cm^{-2} ± 9×10^{-10} A cm^{-2} at -40 °C. At 200 V, the leakage current density reduced from

417 1.989×10^{-6} A cm^{-2} ± 0.007×10^{-6} A cm^{-2} at 140 °C to 2.5×10^{-8} A cm^{-2} ± 0.1×10^{-8} A cm^{-2}
418 at -40 °C.
419
420 It is informative to compare these leakage current densities with those reported previously for
421 Au/4H-SiC Schottky diodes [9]. At a temperature of 100 °C and an applied electric field
422 strength of 103 kV cm^{-1}, the Au/4H-SiC Schottky diodes had a leakage current density ~ 10^{-9}
423 A cm^{-2} [9]; in the same conditions, D3 had a leakage current density of 9.6×10^{-9} A cm^{-2} ±
424 0.9×10^{-9} A cm^{-2}.
425

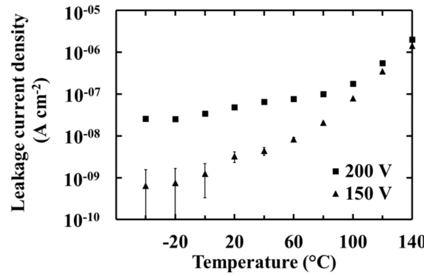

426
427 Figure 9. Leakage current density of D3 as a function of temperature, at 150 V applied
428 reverse bias (corresponding to an applied electric field strength of ≈ 330 kV cm^{-1}) (▲) and
429 200 V applied reverse bias (corresponding to an applied electric field strength of ≈ 370 kV
430 cm^{-1}) (■).
431
432 It is known that the presence of an inhomogeneous barrier can be inferred from investigations
433 of the temperature dependence of the barrier height and the ideality factor [32-33]. Indeed,
434 the results of previously reported NiSi/4H-SiC Schottky diodes used for X-ray spectroscopy
435 suggested such an inhomogeneous barrier [12]. The saturation current, barrier height, and
436 ideality factor of D3 were thus calculated as previously described at each investigated
437 temperature; the results are presented in **Figure 10**. The saturation current of the detector
438 (**Figure 10 (a)**) decreased as the temperature was reduced, from 4.17×10^{-11} A ± 0.03×10^{-11}
439 A at 140 °C to 4.9×10^{-22} A ± 0.3×10^{-22} A at -40 °C. The barrier height and the ideality
440 factor of the detector were found to be temperature invariant, within the investigated
441 temperature range. As shown in **Figure 10 (b)**, the barrier height was 1.18 eV ± 0.01 eV at
442 140 °C, 1.16 eV ± 0.1 eV at 20 °C, and 1.15 eV ± 0.06 eV at -40 °C, with a mean value of
443 1.17 eV ± 0.01 eV (rms deviance) across all temperatures. Since the experimental
444 uncertainties associated with the measurements across the temperature range 40 °C to -40 °C
445 were greater than the rms uncertainty, the mean barrier height was considered to have an
446 uncertainty quantified by the experimental uncertainty of the mean, i.e. ± 0.03 eV. The
447 barrier height of D3 at room temperature, as determined in the initial measurements, was 1.2
448 eV ± 0.1 eV (**Figure 6**). The ideality factor (**Figure 10 (c)**) was 1.04 ± 0.01 at 140 °C, 1.05 ±
449 0.02 at 20 °C, and 1.04 ± 0.02 at -40 °C, with a mean value of 1.03 ± 0.01 (rms deviance)
450 across all temperatures. The uncertainty as quantified by the experimental uncertainty of the
451 mean of the ideality factor was also calculated to be 0.01. The ideality factor of D3 at room
452 temperature was 1.02 ± 0.02 (**Figure 7**). Across this temperature range, the barrier height

Journal Pre-proof

Journal Pre-proof

and the ideality factor display little variance, suggesting a more homogeneous barrier compared to previous NiSi/4H-SiC Schottky diodes [12].

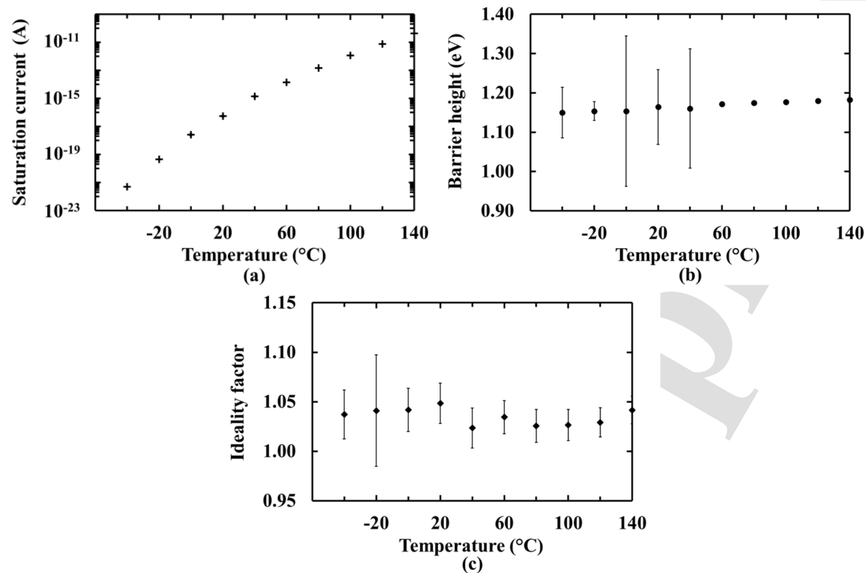

Figure 10. The temperature, T, dependence (140 °C ≤ T ≤ -40 °C) of the (a) saturation current, (b) barrier height, and (c) ideality factor of diode D3.

3. 3. Capacitance measurements

The capacitances of the six Mo/4H-SiC Schottky diodes at room temperature as functions of applied reverse applied bias, are presented in **Figure 11**. All data are displayed in **Figure 11 (a)** and then, for clarity, the capacitances of the diodes at no applied reverse bias and at two selected applied reverse biases (150 V; 200 V), at room temperature, are shown in **Figure 11 (b)** and **Figure 11 (c)**, respectively. It should be noted that the reported capacitances corresponded to the depletion layer capacitance of each Schottky diode; the packaging capacitance, including an estimate of the additional packaging capacitance from the bondwires, was subtracted. The uncertainties associated with the reported depletion layer capacitances were a combination of the uncertainties related to the: accuracy of the LCR meter; repeatability; changed interconnections; and uncertainty associated with the packaging capacitance. The total uncertainty associated with the reported depletion layer capacitances was estimated to be ± 0.1 pF. However, the depletion layer capacitance variations with temperature and/or applied reverse bias had an estimated relative uncertainty of ± 0.007 pF to ± 0.015 pF, since they resulted from a single set of measurements.

Journal Pre-proof

477

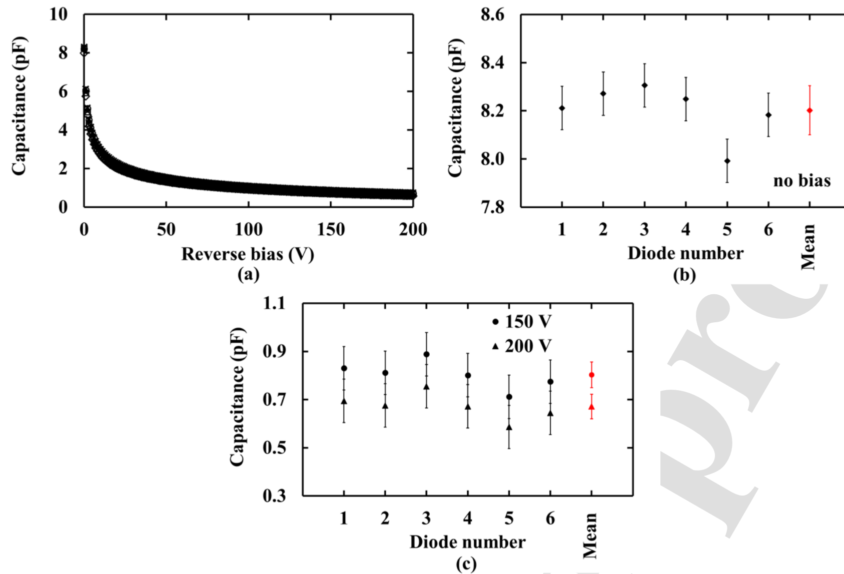

478
479 Figure 11. Depletion layer capacitance (a) of the six Mo/4H-SiC Schottky diodes (D1 (○); D2
480 (▲); D3 (×); D4 (□); D5 (◇); D6 (—)) as a function of applied reverse bias and of the six
481 Mo/4H-SiC Schottky diodes (b) with no applied bias and (c) at 150 V (●) and 200 V (▲), at
482 room temperature. The error bars in (a) were omitted for clarity.
483
484 The depletion layer capacitance of all diodes at room temperature reduced as the applied
485 reverse bias increased from 0 V to 200 V; it did not saturate up to the maximum investigated
486 applied reverse bias. The depletion layer capacitance of all six diodes with no applied bias
487 ranged between 8.0 pF ± 0.1 pF for D5 (minimum) and 8.3 pF ± 0.1 pF for D3 (maximum),
488 with a mean value of 8.2 pF ± 0.1 pF (rms deviance). Although the rms uncertainty was
489 similar to the experimental uncertainties associated with the measurements (± 0.1 pF), D5
490 had a slightly smaller capacitance with no applied bias compared to the rest of the diodes (see
491 **Figure 11 (b)**), potentially due to slight inhomogeneities between D5 and the other devices;
492 the rest of the diodes had the same capacitance at no applied bias, within uncertainties. The
493 depletion layer capacitance of all six diodes at 150 V and 200 V, at room temperature, was
494 also the same, within uncertainties. A mean depletion layer capacitance of 0.80 pF ± 0.05 pF
495 at 150 V and of 0.67 pF ± 0.05 pF at 200 V applied reverse bias was measured. Having
496 established that the capacitance characteristics as a function of applied reverse bias were
497 uniform across the six diodes, the capacitance characteristics of one representative device
498 (D3, as per Section *3. 2. Current measurements*) were then investigated as a function of
499 temperature, 140 °C ≤ T ≤ -40 °C.
500
501 Measurements of the depletion layer capacitance of the Schottky diodes were made not only
502 to allow quantification of part of the noise of the spectrometer, but also to establish the
503 depletion layer width and effective carrier concentration of the diodes. The depletion layer

Journal Pre-proof

504 capacitance of D3 at no applied reverse bias and as a function of temperature is shown in
505 **Figure 12**.
506

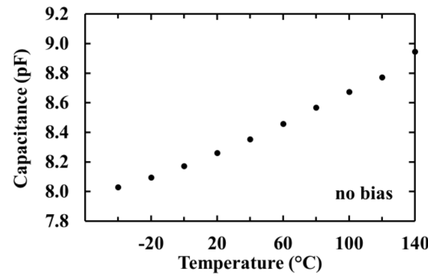

507
508 Figure 12. Depletion layer capacitance of D3 with no applied bias, within the temperature
509 range 140 °C to -40 °C. The uncertainties were smaller than the symbol size.
510

511 The depletion layer capacitance of D3 with no applied bias decreased as the temperature was
512 decreased from 140 °C to -40 °C. It was 8.95 pF ± 0.02 pF at 140 °C and 8.03 pF ± 0.01 pF
513 at -40 °C. However, this was not the case for the depletion layer capacitance of D3 under
514 applied reverse bias. A temperature invariant depletion layer capacitance was measured for
515 D3 when reverse biased at 100 V (e.g. 0.997 pF ± 0.008 pF at 140 °C and 1.007 pF ± 0.008
516 pF at -40 °C), at 150 V (0.826 pF ± 0.007 pF at 140 °C and 0.812 pF ± 0.007 pF at -40 °C),
517 and at 200 V (0.697 pF ± 0.007 pF at 140 °C and 0.689 pF ± 0.007 pF at -40 °C). This
518 observation was further studied by calculating the depletion layer width and exploring its
519 variance with applied reverse bias and temperature. A parallel plate capacitance was
520 assumed to describe the depletion layer capacitance; the depletion layer width was then
521 calculated from the depletion layer capacitance [16]. The depletion layer capacitance and the
522 calculated depletion layer width of D3 as a function of applied reverse bias, at three
523 temperatures (140 °C; 20 °C; -40 °C) is reported in **Figure 13**. The temperature invariance of
524 the capacitance of D3 under applied reverse biases is shown in **Figure 13 (a)**.
525

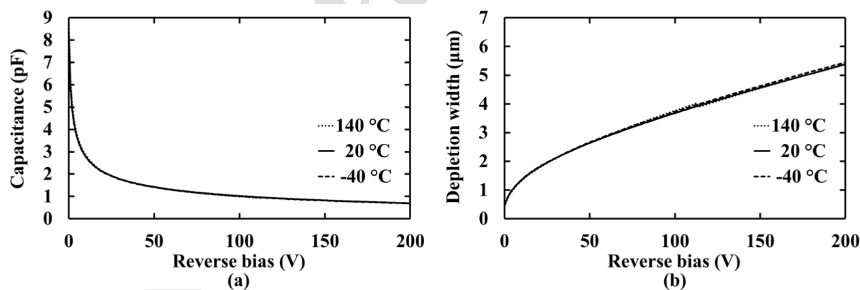

526
527 Figure 13. (a) Depletion layer capacitance and (b) depletion layer width of D3 as a function
528 of applied reverse bias, at 140 °C (···), 20 °C (—), and -40 °C (---). The uncertainties were
529 smaller than the line width.
530

Journal Pre-proof

531 The depletion layer width of D3 at no applied bias varied with temperature; it increased from
532 0.420 μm ± 0.001 μm at 140 °C, to 0.454 μm ± 0.001 μm at 20 °C, and to 0.468 μm ± 0.001
533 μm at -40 °C. As would be expected from the measured depletion layer capacitances, the
534 depletion layer width of D3 was temperature invariant when under the application of
535 significant reverse bias; e.g. at 150 V applied reverse bias, the depletion layer width was 4.6
536 μm ± 0.6 μm (4.55 μm ± 0.04 μm at 140 °C and 4.62 μm ± 0.04 μm at -40 °C). The depletion
537 layer width increased as the applied reverse bias increased and it did not saturate even at the
538 maximum investigated applied reverse bias. The maximum depletion layer width of D3
539 (achieved at 200 V applied reverse bias) and was 5.39 μm ± 0.05 μm at 140 °C and 5.45 μm
540 ± 0.05 μm at -40 °C (i.e. it was temperature invariant).
541
542 The observed dependence of the depletion layer width (and capacitance) at no, and low in
543 other cases, applied reverse bias on temperature has also been reported for other 4H-SiC
544 Schottky diodes [12][34]. This may be explained, at least in part, by the progressive
545 ionization of non-ionized donors with temperature in a thin region around the depletion layer.
546 At no (and low) applied reverse biases, the width of the depletion layer is relatively thin and
547 thus comparable to the thickness of the layer with the non-ionized (at low temperatures)
548 donors. In contrast, at high applied reverse biases, and as the depletion layer widens, the
549 contribution of this possible thin layer around the depletion layer becomes less significant.
550
551 The effective carrier concentration within the n^- epitaxial layer was then calculated. The
552 effective carrier concentration can be approximated to the majority carrier concentration, can
553 be extracted from the capacitance measurements, with a spatial resolution of the order of a
554 Debye length (0.05 μm in this case, [16]). The differential capacitance method, which is
555 suitable for a non-constant carrier concentration throughout the depletion region [16] was
556 used. The results for D3, at three temperatures (140 °C; 20 °C; -40 °C) are presented in
557 **Figure 14**. Although the 35 μm thick n^- epitaxial layer of the Mo/4H-SiC Schottky diodes
558 was thought to be lightly doped at 1×10^{15} cm^{-3} based on indications from the epitaxy, the
559 capacitance measurements of D3 suggested a higher effective carrier concentration. The
560 effective carrier concentration of D3 at 20 °C at 5.4 μm ± 0.8 μm (at 200 V) below the
561 Schottky junction was 7×10^{15} cm^{-3} ± 3×10^{15} cm^{-3}. The effective carrier concentration as
562 determined (7×10^{15} cm^{-3} ± 3×10^{15} cm^{-3}) was higher than expected (1×10^{15} cm^{-3}) given the
563 specifications quoted by the manufacturer; the difference could be attributable to additional
564 packaging capacitances which were not subtracted, but the amount of extra stray capacitance
565 which would be required (0.32 pF) appears to be greater than can be attributed reasonably to
566 any part of the system. An alternative explanation would be that the carrier concentration of
567 the material was indeed greater than that specified by the manufacturer. The results shown in
568 **Figure 11 (C)** (i.e. that the depletion layer capacitance of all six diodes at 150 V and 200 V,
569 at room temperature, was the same within uncertainties) suggested that the effective carrier
570 concentration of all six diodes at 20 °C was the same as that extracted for D3.
571

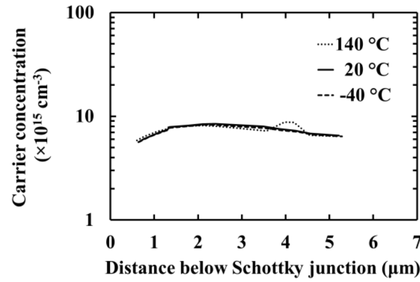

572
573 Figure 14. Carrier concentration within the n⁻ epitaxial layer of D3 as a function of distance
574 bellow the Schottky junction, at 140 °C (···), 20 °C (—), and -40 °C (---). Measurements of
575 the capacitances of all six diodes suggest that all devices had the same effective carrier
576 concentration at 20 °C.
577
578 The expected depletion layer width at > 200 V applied reverse bias was then calculated,
579 based on the effective carrier concentration within the n^- epitaxial layer (7×10^{15} cm^{-3} at 5.4
580 µm below the Schottky junction) as determined from the capacitance measurements [16]. A
581 depletion layer width of 35 µm at 20 °C was predicted to be achieved at 8000 V applied
582 reverse bias (2.3×10^{6} V cm^{-1}), assuming the carrier concentration at distances ≥ 5.4 µm
583 below the Schottky junction was as had been determined for shallower depths.
584
585 *3. 4. X-ray and γ-ray spectroscopy measurements*
586 An example ^{55}Fe X-ray spectrum accumulated at room temperature using D2 is presented in
587 **Figure 15**. For the spectrum shown, the detector was operated at 150 V applied reverse bias
588 and the shaping amplifier was operated with a shaping time of 1 µs. The Mn Kα (at 5.9 keV)
589 and Mn Kβ (at 6.49 keV) characteristic X-ray emissions of the ^{55}Fe radioisotope X-ray source
590 were not individually resolved. Instead, the detected photopeak was their combination. The
591 separate contributions of the Mn Kα and Kβ emissions were deconvolved allowing the
592 quantification of the FWHM at 5.9 keV. Two Gaussians were computed in each case, one for
593 Mn Kα and one for Mn Kβ, taking into account the characteristic energies, their relative
594 emission ratio, and the ratio of the quantum detection efficiencies of the detector at the two
595 characteristic energies. The summation of the two Gaussians was then fitted to the combined
596 photopeak of each spectrum. The centroid channel number of the ≈ 0 keV noise peak of the
597 CSP and that of the fitted Mn Kα photopeak, along with their respective energies, were used
598 to energy calibrate the MCA charge scale of each spectrum. The Full Width at Half
599 Maximum, FWHM, of the Mn Kα (5.9 keV) peak was 1.67 keV ± 0.08 keV for the spectrum
600 presented. Partial collection of charge created in the non-active layers of the detector resulted
601 in the low energy tailing at the left hand side of the combined Mn Kα and Mn Kβ X-ray
602 photopeak, shown in **Figure 15**. Having established the position of the CSP noise peak
603 during the first few (real time) seconds of each spectrum, the MCA low energy cut-off
604 (threshold) channel number was set at > 0 keV in order to limit the counts of the noise peak;
605 the right hand side of the tail of the 0 keV noise peak, which was above the MCA low energy
606 cut-off channel number set, can be seen in combination with counts arising from partial

Journal Pre-proof

Journal Pre-proof

607 charge collection at the low energy side of the Mn Kα and Kβ photopeak, as well as possibly
608 a combined Ag Lα and Lβ peak (package fluorescence) at ≈ 3 keV (e.g. see **Figure 15**).
609

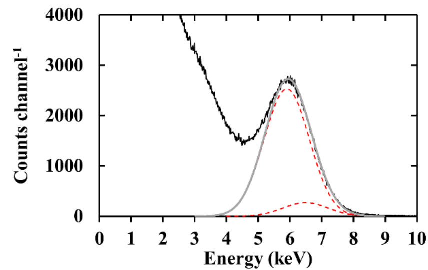

610
611 Figure 15. ^{55}Fe X-ray spectrum (—) accumulated with the D2 based spectrometer (150 V
612 applied reverse bias; 1 µs shaping time) at room temperature. The Gaussian peaks fitted at
613 the Mn Kα and Kβ lines (---) and their summation (—) are also shown. The Full Width at
614 Half Maximum of the Mn Kα (5.9 keV) peak was 1.67 keV ± 0.08 keV.
615
616 The FWHM at 5.9 keV was deduced for each of the accumulated ^{55}Fe radioisotope X-ray
617 spectra. The results are provided in **Figure 16**. At each investigated applied reverse bias, the
618 FWHM improved as the shaping time lengthen from 0.5 µs to the optimum shaping time, and
619 degraded for a further lengthening of the shaping time. The best FWHM at 5.9 keV was 1.72
620 keV ± 0.08 keV (2 µs) at 50 V, 1.67 keV ± 0.07 keV (2 µs) at 100 V, and 1.67 keV ± 0.08
621 keV (1 µs) at 150 V applied reverse bias. It can thus be concluded that the best achievable
622 FWHM at 5.9 keV was the same at all three investigated applied reverse biases. However, it
623 should be noted that the shaping time to achieve this did vary when considering the
624 uncertainties of the FWHM associated with the Gaussian fitting; the best achievable FWHM
625 was obtained at shaping times, τ, 2 µs ≤ τ ≤ 6 µs at 50 V and 1 µs ≤ τ ≤ 3 µs at both 100 V and
626 150 V. To provide a better insight into the different noise components contributing to the
627 observed FWHM at 5.9 keV, an analysis of the noise contributors was conducted for the
628 system.
629

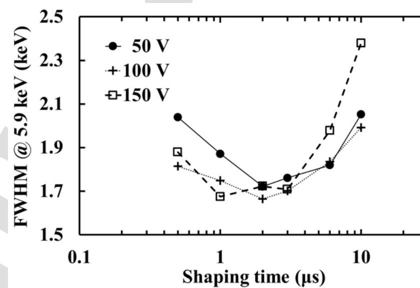

630
631 Figure 16. FWHM at 5.9 keV as a function of shaping time at all three investigated applied
632 reverse biases: 50 V (●); 100 V (+); 150 V (□). The error bars, ranging from ± 0.07 keV to ±
633 0.2 keV, were omitted for clarity. The lines are guide to the eyes only.
634

Journal Pre-proof

635 The broadening of the photopeaks in the detected spectra is due to noises arising in the
636 detector and the CSP [35]. The three noise components (which are summated in quadrature
637 to result in the total noise) of a non-avalanche semiconductor detector based X-ray and/or γ-
638 ray spectrometer are the Fano noise, the incomplete charge collection (ICC) noise, and the
639 electronic noise. The first two noise components arise exclusively within the detector: the
640 Fano noise arises due to stochastic fluctuations in the number of electron-hole pairs generated
641 per unit of photon energy; the ICC noise, if any is present, arises due to trapping and/or
642 recombination of the generated electrons and holes created, typically at the crystal
643 imperfections of the detector. The electronic noise, comprising white parallel (WP) noise,
644 white series (WS) noise (including the induced gate current noise), $1/f$ noise, and dielectric
645 (DL) noise, arises due to the semiconductor detector and the CSP and their coupling. An
646 introduction to the electronic noise components is provided by Bertuccio et al. [36] and
647 Lioliou and Barnett [35].
648
649 For the present spectrometer, the different noise components vary in different manners with
650 the operating conditions (the shaping time, the reverse bias of the detector, the temperature,
651 and the incoming photon energy) of the spectrometer. It is informative to note the
652 relationship of each noise component with the shaping time, τ. The total equivalent noise
653 charge (ENC), N, measured in e^- rms, is expressed as
654

655 $$N^2 = A\frac{1}{\tau} + B\tau + C \quad (1)$$

656
657 where A, B, and C are the parameters representing the white series noise contribution, the
658 white parallel noise contribution, and the rest of the noise contributions, respectively [37].
659 Thus, a multidimensional nonlinear least squares fitting of the total measured equivalent
660 noise charge as a function of shaping time allowed the quantification of the three parameters
661 of Eq. (1). The multidimensional least squares fitting of the experimentally measured $N(\tau)$ at
662 the three investigated applied reverse biases can be seen in **Figure 17**. The parameter C of
663 the fitting represented all the noise components that were shaping time invariant, namely: the
664 Fano noise; $1/f$ noise; dielectric noise; and incomplete charge collection noise. The Fano
665 noise and the $1/f$ noise were calculated and their combined contribution was subtracted in
666 quadrature from the total shaping time invariant contribution. The result was the quadratic
667 sum of the dielectric and (if any was present) the incomplete charge collection noise, see
668 **Figure 17**. To do this, the Fano noise was calculated, assuming a Fano factor of 0.1 and an
669 average electron hole pair creation energy of 7.8 eV [9] for 4H-SiC; it was 8.7 e^- rms (160
670 eV) at 5.9 keV. The $1/f$ noise contribution was computed using the total capacitance
671 estimated from the parameter A of the multidimensional nonlinear fitting; it was found to be
672 < 10 e^- rms [35].
673

674

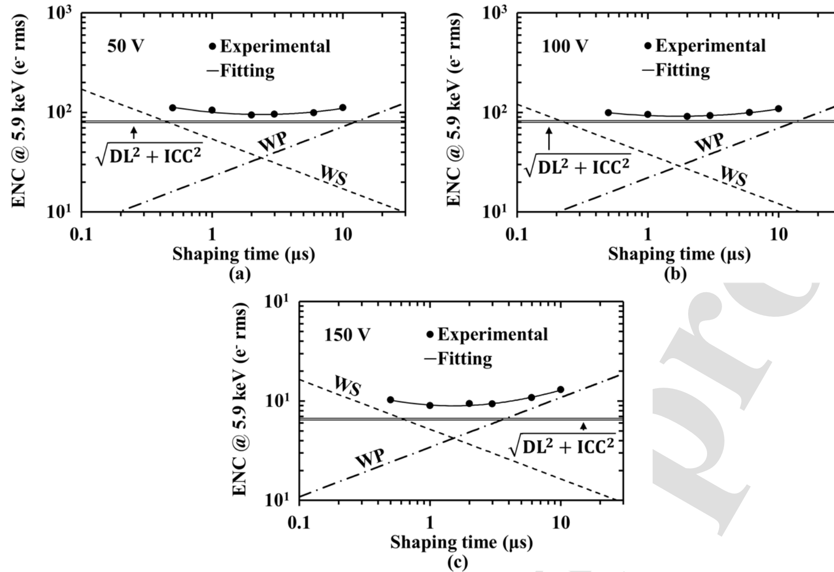

675
676 Figure 17. ENC at 5.9 keV (●) at: (a) 50 V; (b) 100 V; and (c) 150 V applied reverse bias as
677 a function of shaping time. The white series (WS) noise, the white parallel (WP) noise, and
678 the quadratic sum of the dielectric (DL) and incomplete charge collection (ICC) noise, as
679 determined from a multidimensional least squares fitting (—) of the experimental data, are
680 also shown.
681
682 The dominant source of noise at 50 V and 100 V applied reverse bias, and across all the
683 investigated shaping times, was the quadratic sum of the dielectric noise and (if any)
684 incomplete charge collection noise. The dielectric noise arose from all lossy dielectrics in
685 close proximity to the input of the preamplifier; these were the detector and its packaging; the
686 feedback capacitance; the passivation, packaging, and dielectrics of the input JFET; and any
687 stray dielectrics [23][36][38]. The combined contribution of the dielectric noise and the
688 incomplete charge collection noise was 81 e^- rms at both 50 V and 100 V applied reverse
689 bias. However, the combined contribution of the dielectric noise and the incomplete charge
690 collection noise (= 66 e^- rms) was the dominant source of noise at 150 V applied reverse bias
691 only within the shaping time, τ, 0.7 μs $\leq \tau \leq$ 3.7 μs. The WS noise dominated at shaping
692 times < 0.7 μs and the WP noise dominated at shaping times > 3.7 μs, at an applied reverse
693 bias of 150 V.
694
695 As discussed above, the uncertainties of the FWHM associated with the Gaussian fitting
696 prevented the identification of a single optimum available shaping time and applied reverse
697 bias, in terms of achieving the best (lowest) FWHM at 5.9 keV. Instead, multidimensional
698 nonlinear least squares fitting of the experimental $N(\tau)$ allowed the determination of the
699 optimum operating conditions (reverse bias applied to the detector and shaping amplifier
700 shaping time) of the spectrometer at room temperature. Initially, the parameters A and B as
701 extracted from the fitting were used to define the optimum shaping time at each applied

Journal Pre-proof

reverse bias. The FWHM at 5.9 keV is minimised at the shaping time where the WS noise and the WP noise are equal. This occurred at 2.4 μs at 50 V, at 1.7 μs at 100 V, and 1.4 μs at 150 V. The optimum shaping time shortened with increased applied reverse bias. This was attributed to the increase of the WP noise contribution of the detector, due to the increase of its leakage current, while the WS noise contribution of the detector reduced, due to its reduced capacitance, as the applied reverse bias increased in magnitude (see **Figure 4** and **Figure 11**). Then, the lowest ENC (at the optimum shaping time) as determined from the fitting of Eq. (1) to the experimental $N(\tau)$ was used to identify the optimum applied reverse bias of the detector, among the three values investigated. This was 95 e^- rms at 50 V, 92 e^- rms at 100 V, and 90 e^- rms at 150 V. It was thus concluded that the optimum available operating conditions of the spectrometer were 150 V applied reverse bias and 1 μs shaping time; these conditions were used during accumulation of the ^{109}Cd and ^{241}Am radioisotope X-ray and γ-ray spectra which subsequently obtained.

The number of counts within the Gaussian fitted to the Mn Kα X-ray peak was determined at the three investigated applied reverse biases (each at 1 μs) in order to investigate any variance with applied reverse bias. The number of counts contained within the Gaussian increased from 215.7×10^3 counts $\pm 0.6 \times 10^3$ counts at 50 V to 265.2×10^3 counts $\pm 0.8 \times 10^3$ counts at 100 V, and to 300.4×10^3 counts $\pm 0.9 \times 10^3$ counts at 150 V. The increase in the number of counts with detector applied reverse bias was consistent with the expected increase of the *QE* as the applied reverse bias increased from 50 V to 150 V, thus suggesting that any improvement of the charge transport (within solely the depletion region present at each reverse bias) as the applied electric field was increased was insignificant (the applied electric field strength increased from ≈ 188 kV cm^{-1} to ≈ 330 kV cm^{-1}); this suggests that any incomplete charge collection within the depletion region itself was likely to be insignificant. The *QE* at 5.9 keV, assuming an active layer thickness equal to the depletion layer width at each applied reverse bias (**Figure 13 (b)**), increased from 0.0853 at 50 V, to 0.1177 at 100 V, and to 0.1406 at 150 V.

The ^{109}Cd radioisotope X-ray and γ-ray spectrum accumulated using the spectrometer is presented in **Figure 18**. The main characteristic X-ray emissions of the ^{109}Cd radioisotope X-ray and γ-ray source, Ag $K\alpha_1$ (22.16 keV), $K\alpha_2$ (21.99 keV), and Kβ (24.9 keV) X-rays, were identified in the spectrum. The characteristic Ag Lα (2.98 keV) X-rays were not resolved from the ≈ 0 keV noise peak of the CSP. The peak corresponding to the γ-ray emission of the ^{109}Cd radioisotope X-ray and γ-ray source, at 88.03 keV, was not formed in the spectrum within the set live time due to the low quantum detection efficiency of the detector at this high photon energy. The combination of the two X-ray fluorescence peaks from the stainless steel capsule of the radioisotope source, at Fe Kα (6.4 keV) and Cr Kα (5.4 keV), was apparent in the spectrum, as was an Au ($L\beta_1$ = 11.4 keV; $L\beta_2$ = 11.6 keV) X-ray fluorescence peak from the detector's packaging.

The main photopeak in the spectrum was the combination of the Ag $K\alpha_1$ (22.16 keV) and $K\alpha_2$ (21.99 keV) emissions. The separate Ag $K\alpha_1$ and $K\alpha_2$ contributions were deconvolved by fitting the summation of two Gaussian peaks to this combined peak. The two Gaussians

746 were calculated considering the characteristic energies, their relative emission ratio, and the
747 ratio of the quantum detection efficiencies of the detector (**Figure 2**) at the two characteristic
748 energies. Then, the centroid channel number of the ≈ 0 keV noise peak of the CSP and that
749 of the Gaussian fitted to the Ag $K\alpha_1$ were used to energy calibrate the MCA charge scale.
750 Similarly to the ^{55}Fe radioisotope X-ray spectra, the counts of the ≈ 0 keV noise peak of the
751 CSP were limited by setting the MCA low energy cut-off at an energy > 0 keV (2.6 keV)
752 once the position of the noise peak had been established. Finally, the FWHM at 22.16 keV
753 was recorded; it was 1.7 keV ± 0.1 keV.
754

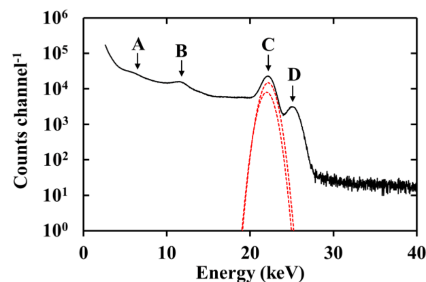

755
756 Figure 18. ^{109}Cd X-ray and γ-ray spectrum accumulated with the spectrometer at room
757 temperature (150 V reverse bias; 1 µs shaping time; FWHM at 22.16 keV = 1.7 keV ± 0.1
758 keV; —). The major X-ray peaks identified are: (A) Cr Kα and Fe Kα capsule fluorescence;
759 (B) Au Lβ packaging fluorescence; (C) ^{109}Cd Ag $K\alpha_1$ and $K\alpha_2$; (D) ^{109}Cd Ag Kβ. The
760 Gaussians fitted representing the Ag $K\alpha_1$ and $K\alpha_2$ peaks are also shown (---).
761

762 The ^{241}Am radioisotope X-ray and γ-ray spectrum accumulated using spectrometer is shown
763 in **Figure 19**. The main characteristic emission lines of the ^{241}Am radioisotope X-ray and γ-
764 ray source (Np Lα (13.76 keV and 13.95 keV), Lβ (ranging from 16.11 keV to 17.99 keV),
765 and Lγ (ranging from 20.78 keV to 21.49 keV) X-rays, and the γ-rays at 26.3 keV and 59.54
766 keV) were all identified in the spectrum. The peaks corresponding to the characteristic γ-rays
767 with the lowest intensities, i.e. at 33.2 keV and 43.4 keV, were not formed sufficiently well
768 so as to be readily distinguished within the set live time. A combined peak of the two X-ray
769 fluorescence peaks from the stainless steel capsule of the radioisotope source (Fe Kα, 6.4
770 keV; Cr Kα 5.4 keV) was visible in the spectrum. A peak at 39.5 keV, hypothesised to be
771 from the detection of K shell photoelectrons (binding energy = 20.0 keV) ejected from the
772 Mo contact upon absorption of ^{241}Am γ_1 γ-rays (59.54 keV) in the contact, was also present;
773 the corresponding Mo Kα ($K\alpha_1$ = 17.5 keV, $K\alpha_2$ = 17.4 keV) and Kβ (19.6 keV) fluorescence
774 X-rays would have been unresolved from the ^{241}Am Np Lβ and Lγ X-ray peaks, respectively.
775

776 The ^{241}Am 59.54 keV γ-ray peak was fitted with a Gaussian peak. Energy calibration of the
777 MCA charge scale was achieved using the centroid channel number of the ≈ 0 keV noise
778 peak of the CSP and that of the Gaussian fitted to the ^{241}Am 59.54 keV γ-ray peak, along with
779 their corresponding energies. Again, the counts of the noise peak were limited by setting the
780 MCA low energy cut-off at 2.6 keV, after establishing the position of the noise peak. The
781 FWHM at 59.54 keV was 1.6 keV ± 0.1 keV.

Journal Pre-proof

Journal Pre-proof

782

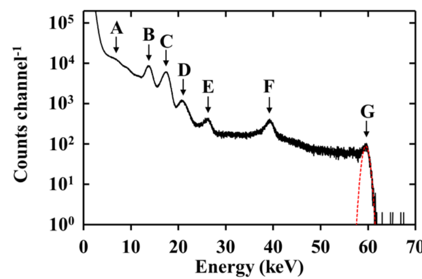

783
784 Figure 19. [241]Am radioisotope X-ray and γ-ray spectrum accumulated with the spectrometer
785 at room temperature (150 V reverse bias; 1 μs shaping time; FWHM at 59.54 keV = 1.6 keV
786 ± 0.1 keV; —). The major peaks identified are: (A) Cr Kα and Fe Kα capsule X-ray
787 fluorescence; (B) [241]Am Np Lα X-ray; (C) [241]Am Np Lβ X-ray and Mo Kα contact X-ray
788 fluorescence; (D) [241]Am Np Lγ X-ray and Mo Kβ contact X-ray fluorescence; (E) [241]Am 26.3
789 keV γ-ray; (F) Mo K shell photoelectron peak at 39.5 keV from [241]Am γ_1 (59.54 keV)
790 absorption in the Mo contact; (G) [241]Am 59.54 keV γ-ray. The Gaussian fitted at the 59.54
791 keV γ-ray peak is also shown (---).
792
793 Summarising for the three radioisotope radiation sources presented, the energy resolution
794 (FWHM) of the spectrometer, operating uncooled at room temperature, was 1.67 keV ± 0.08
795 keV at 5.9 keV, 1.7 keV ± 0.1 keV at 22.16 keV, and 1.6 keV ± 0.1 keV at 59.54 keV. These
796 values corresponded to a total ENC of 97 e^- rms ± 5 e^- rms at 5.9 keV, 99 e^- rms ± 6 e^- rms at
797 22.16 keV, and 93 e^- rms ± 6 e^- rms at 59.54 keV. It was thus concluded that the noise
798 present was constant, within uncertainties, across the investigated photon energy, *E*, range,
799 5.9 keV $\leq E \leq$ 59.54 keV, even though the Fano noise increased with increasing energy. The
800 Fano noise was calculated to be 9 e^- rms (160 eV) at 5.9 keV, 17 e^- rms (400 eV) at 22.16
801 keV, and 28 e^- rms (508 eV) at 59.54 keV. The apparent constancy of the FWHM as a
802 function of energy arises from the size of the uncertainties associated with the measurements
803 and the relatively high total noise which is far greater than the Fano noise alone. The absence
804 of an energy dependence in the achieved FWHM as a function of photon energy indicates
805 that if there was any ICC noise, its contribution was small compared with the other noise
806 contributors; nevertheless, it cannot be stated conclusively that the ICC noise was nil.
807
808 To make clear the impact of the average electron-hole pair creation energy, ω, it is
809 informative to compare the energy resolutions achievable with spectrometers employing
810 detectors made from different semiconductor materials. Whilst the total ENC of a
811 spectrometer depends in part upon the detector itself, it is useful for this purpose to compare
812 different detector materials assuming a consistent total ENC for their respective
813 spectrometers. Assuming an ENC of 97 e^- rms ± 5 e^- rms (i.e. equal to that measured at 5.9
814 keV for the reported spectrometer), the FWHM which would be achieved using detectors
815 made from Si (ω = 3.67 eV [39]) and GaAs (ω = 4.184 eV [40]) would be 0.84 keV ± 0.04
816 keV and 0.96 keV ± 0.05 keV, respectively. Thus, developing ultra-low noise preamplifier

Journal Pre-proof

817 electronics for 4H-SiC detector spectrometers is of a higher importance cf. developing such
818 electronics for spectrometers using Si detectors.
819
820 However, depending on environmental conditions and detector characteristics, the ENC
821 contributions of detectors made from different materials can be significantly disparate. For
822 example, at high temperatures, large thermally generated leakage currents can lead to the
823 total spectrometer ENC being dominated by PW noise contributions when using a narrower
824 bandgap detector; in contrast, the thermally generated leakage current would not be so high if
825 a wider bandgap detector was used. The exact physical nature of the relationship between
826 semiconductor bandgap, E_g, and ω is still subject to study [41-42] but it appears that $\omega \propto E_g$.
827 Consequently, even though a wide bandgap detector material (with a large ω) may be at a
828 disadvantage cf. a narrower bandgap detector (with a small ω) at low temperatures, at high
829 temperatures the wider bandgap of the detector with the larger ω may be sufficiently
830 advantageous as to outweigh the larger ω [43]. It should be noted that both E_g and ω are
831 temperature dependent.
832
833 The energy resolution achieved with the Mo/4H-SiC Schottky diode detector spectrometer is
834 similar to that achieved with other previously reported 4H-SiC detector spectrometers,
835 employing similar preamplifier electronics. Notable examples include: a FWHM at 22 keV
836 of 1.47 keV at 23 °C achieved with an early semi-transparent NiSi/4H-SiC Schottky diode
837 [10]; a FWHM at 5.9 keV of 1.5 keV at 20 °C achieved with another generation of NiSi/4H-
838 SiC Schottky diode detector [11]; a FWHM at 17.4 keV of 1.36 keV at 30 °C which was
839 achieved with another type of NiSi/4H-SiC Schottky diode [12]; a FWHM at 5.9 keV of 1.26
840 keV at 20 °C achieved with a recent Ni_2Si/4H-SiC Schottky diode [13]; and a FWHM at 5.9
841 keV of 1.66 keV ± 0.15 keV at 20 °C achieved with a commercial UV 4H-SiC p-n
842 photodiode repurposed for X-ray detection [15]. However, all of these energy resolutions are
843 substantially poorer than was achieved with a Au/4H-SiC Schottky diode and exceptionally
844 low-noise preamplifier electronics (3 e^- rms ENC, when unloaded, at room temperature): with
845 this detector, a FWHM at 5.9 keV of 196 eV at 30 °C was reported [9]. Thus, the importance
846 of employing electronics with minimal noise contribution in 4H-SiC detector based
847 spectrometers is emphasized again.
848
849 The importance of the (Schottky and Ohmic) contact material, the methods of surface
850 processing/preparation, and the techniques for contact formation on the performance of X-ray
851 and γ-ray spectroscopic detectors has been investigated by previous comparative studies on
852 CdTe detectors, using commercial detector-grade p-like CdTe semiconductor crystals. TiO_x
853 Schottky contacts and MoO_x Ohmic contacts were formed by DC reactive magnetron
854 sputtering; the resultant TiO_x/p-CdTe/MoO_x detector based spectrometer had 10.9 keV (18.3
855 %) FWHM at 59.54 keV, at room temperature [44]. Different Schottky contacts and methods
856 for contact formation were also investigated; MoO_x, TiN, and In were formed on p-CdTe
857 [45]. The energy resolution of these spectrometers varied from 3 keV (5 %) to 12 keV (20
858 %) FWHM at 59.54 keV at room temperature, highlighting the importance of developing a
859 deep understanding of the effects of the contact material, surface processing, and contact

Journal Pre-proof

860 deposition on the charge carrier transport mechanisms and hence the performance of X-ray
861 and γ-ray spectroscopic detectors [44] [45].
862
863 **4. Conclusions**
864 For the first time, Mo/4H-SiC Schottky diodes have been investigated for their suitability as
865 photon counting detectors for X-ray and γ-ray spectroscopy. The diodes had 35 µm thick n^-
866 type epilayers and were P_2O_5 passivated. Measurements and calculations of parameters
867 relating to the electrical characteristics of diodes were reported for six devices, D1 – D6, at
868 room temperature, and for one representative device, D3, at temperatures -40 °C ≤ T ≤ 140
869 °C. One randomly selected device, D2, was then used to accumulate X-ray and γ-ray spectra
870 of three radioisotope radiation sources, at room temperature.
871
872 The quantum detection efficiency, *QE*, of the devices across the energy range of interest was
873 first explored. It was computed that when the devices were reverse biased at 150 V, the
874 depletion width was 4.6 µm. This indicated *QE* of 0.1406, 0.0031, 0.00014, and 0.00004 at
875 5.9 keV, 22.16 keV, 59.54 keV, and 88.03 keV, respectively. Had the 35 µm thick n^- type
876 epilayer been fully depleted, the *QE* would have been 0.6638, 0.0235, 0.0010, and 0.0003 at
877 the same energies.
878
879 Electrical characterization showed that the leakage currents of D1 – D6 were the same, within
880 uncertainties, up to an applied reverse bias of 140 V, at room temperature. However, at
881 applied reverse bias > 140 V, and at applied forward biases, the devices' current differed.
882 These reverse biases correspond to extremely high electric field strengths. The leakage
883 current densities were calculated. At 100 V applied reverse bias (≈ 265 kV cm^{-1}), they were
884 found to be the same across all devices, with a mean value of 5×10^{-10} A cm^{-2} ± 2×10^{-10} A
885 cm^{-2} (rms deviance). However, at 200 V applied reverse bias (≈ 370 kV cm^{-1}), it ranged
886 from 0.73×10^{-7} A cm^{-2} ± 0.01×10^{-7} A cm^{-2} for D4 (the minimum) to 3.19×10^{-7} A cm^{-2} ±
887 0.02×10^{-7} A cm^{-2} for D6 (the maximum). The diodes, D1 – D6, had the same barrier height
888 (1.23 eV ± 0.03 eV) and ideality factor (1.01 ± 0.01) at room temperature.
889
890 High quality Au/4H-SiC Schottky diodes have been reported previously to have very low
891 leakage current densities of ~ 10^{-12} A cm^{-2} at 103 kV cm^{-1} at room temperature [9]; the
892 Mo/4H-SiC devices had comparable leakage current densities (≤ 84×10^{-12} A cm^{-2}) under
893 the same conditions. The low leakage current densities of the Mo/4H-SiC Schottky diodes
894 was attributable in part to the P_2O_5 surface passivation [21-22] as well as to the high quality
895 epitaxial material. Mo/4H-SiC detector D3 was characterised at high temperature; it had a
896 leakage current density of 9.6×10^{-9} A cm^{-2} ± 0.9×10^{-9} A cm^{-2} at 100 °C; this was again
897 comparable to that reported for Au/4H-SiC Schottky detectors operated under the same
898 conditions (1×10^{-9} A cm^{-2} at 100 °C). The electrical characterisation as a function of
899 temperature showed an absence of a dependency of the barrier height and the ideality factor
900 upon temperature, thus suggesting an homogeneous barrier.
901
902 The devices were not fully depleted even at the maximum applied reverse bias (200 V),
903 although they had the same depletion layer capacitance at 150 V and 200 V, within

Journal Pre-proof

904 uncertainties. The depletion layer capacitance of D3 at no applied bias decreased as the
905 temperature was decreased from 140 °C (8.95 pF ± 0.02 pF) to -40 °C (8.03 pF ± 0.01 pF).
906 However, a temperature invariant depletion layer capacitance was measured for D3 when it
907 was reverse biased. The depletion layer width of D3 at 150 V applied reverse bias, at 20 °C,
908 was 4.6 μm ± 0.6 μm. The only partial depletion of the n^- epitaxial layer, even at high
909 applied field strengths, was attributed to a relatively high effective carrier concentration in the
910 material (7×10^{15} cm^{-3} ± 3×10^{15} cm^{-3}).
911
912 One Mo/4H-SiC detector, D2, was coupled to radiation spectrometer readout electronics.
913 The detector and readout chain were operated at room temperature. The detector was
914 illuminated with ^{55}Fe, ^{109}Cd, and ^{241}Am radioisotope X/γ -ray sources. FWHM at 5.9 keV of
915 1.72 keV ± 0.08 keV (2 μs shaping time; 50 V applied reverse bias), 1.67 keV ± 0.07 keV (2
916 μs; 100 V), and 1.67 keV ± 0.08 keV (1 μs; 150 V) were achieved; by modifying the shaping
917 time the same energy resolution could be achieved at each of the three detector reverse biases
918 investigated. However, the dominant source of noise was a function of both the applied
919 reverse bias and shaping time. The dominant source of noise at 50 V and 100 V applied
920 reverse bias, and across all the investigated shaping times, was the quadratic sum of the
921 dielectric noise and (if any) incomplete charge collection noise. The combined contribution
922 of the dielectric noise and the incomplete charge collection noise (if any) was the dominant
923 source of noise at 150 V applied reverse bias only within the shaping time, τ, 0.7 μs ≤ τ ≤ 3.7
924 μs; the WS noise dominated at shaping times < 0.7 μs, and the WP noise dominated at
925 shaping times > 3.7 μs. The combined contribution of the dielectric noise and (if any)
926 incomplete charge collection noise reduced from 81 e^- rms at both 50 V and 100 V to 66 e^-
927 rms at 150 V. The noise analysis suggested that the optimum available operating conditions
928 of the D2 based spectrometer at room temperature were 150 V applied reverse bias and 1 μs
929 shaping time. It should be noted that whilst care has been taken to state that it is possible that
930 incomplete charge collection noise contributed to the noise, no increase in FWHM as a
931 function of photon energy was found in the data; this suggested that any incomplete charge
932 collection noise that was present was insignificant compared to the dielectric noise itself.
933
934 ^{109}Cd and ^{241}Am radioisotope X-ray and γ-ray spectra were accumulated using the same
935 device at room temperature, 150 V applied reverse bias, and 1 μs shaping time. Energy
936 resolutions of 1.7 keV ± 0.1 keV FWHM at 22.16 keV (Ag Kα, from ^{109}Cd) and 1.6 keV ±
937 0.1 keV FWHM at 59.54 keV (^{241}Am γ_1) were measured. Within the limitations of the
938 achieved energy resolutions, all of the main characteristic X-ray and γ-ray emissions of the
939 two radioisotope radiation sources were detected except for: the 88.03 keV γ-ray emission of
940 the ^{109}Cd radioisotope X-ray and γ-ray source (not detected due to low *QE* of the detector at
941 this energy); and the 33.2 keV and 43.4 keV γ-ray emissions of the ^{241}Am radioisotope X-ray
942 and γ-ray source (not detected due to the combination of their low emission rates and the
943 relatively low QE of the detector).
944
945 In summary, for the first time, it has been demonstrated that Mo/4H-SiC Schottky diodes can
946 be used for X-ray and γ-ray photon counting spectroscopy. Until recently, the informed
947 detector designer may have concluded that Mo/4H-SiC Schottky diodes were likely to be of

Journal Pre-proof

948 limited applicability for X-ray and γ-ray detection given that their relatively low barrier
949 heights (a result of the work function of Mo) may have led to high leakage current densities.
950 However, the devices presented here were P_2O_5 passivation; a technique suggested to affect
951 the contact subsurface by homogenising the interface [22]. Indeed, the performance of the
952 Mo/4H-SiC Schottky diodes for X-ray and γ-ray spectroscopy was found to not be limited by
953 the leakage current of the detector, apart from at high reverse biases when utilising long
954 shaping times (> 3.7 μs). The results open new pathways for the consideration of Mo/4H-SiC
955 Schottky diodes in X-ray and γ-ray spectroscopy; the suitability of the detectors will be
956 investigated further and their development pursued and reported in future publications.
957

958 **ACKNOWLEDGEMENTS**

959 This work was supported, in part, by Science and Technology Facilities Council, UK,
960 through grants ST/R000247/1 and ST/T000910/1 (University of Sussex, A.M.B., PI).
961 A.M.B. acknowledges funding from the Leverhulme Trust, United Kingdom, in the form of a
962 2016 Philip Leverhulme Prize. Development of the devices was supported by Engineering
963 and Physical Sciences Research Council, UK, through grant EP/R00448X/1 (University of
964 Warwick, P.M.G., PI). Fabrication of the devices was supported, in part, by Engineering and
965 Physical Sciences Research Council, UK, through grant EP/P017363/1 (University of
966 Warwick, V.A.S., PI).
967

968 **DATA AVAILABILITY**

969 All data that support the findings of this study are included within the article.
970

971 **REFERENCES**

972 [1] O. Madelung, Semiconductors: Group IV Elements and III-V Compounds, Springer,
973 Berlin, 1991.
974 [2] G. Bertuccio, D. Puglisi, D. Macera, R. Di Liberto, M. Lamborizio, L. Mantovani, Silicon
975 Carbide Detectors for in vivo Dosimetry, IEEE Transactions on Nuclear Science, 61 (2014)
976 961-966.
977 [3] S. Yu. Davydov, On the Electron Affinity of Silicon Carbide Polytypes,
978 Semiconductors, 41 (2007)696-698.
979 [4] M.E. Levinshtein, S.L. Rumyantsev, M.S. Shur, Properties of Advanced Semiconductor
980 Materials: GaN, AIN, InN, BN, SiC, SiGe, John Wiley & Sons, Chichester, 2001.
981 [5] A.A. Lebedev, V.V. Kozlovski, N.B. Strokan, D.V. Davydov, A.M. Ivanov, A.M.
982 Strel'chuk, R. Yakimova, Radiation hardness of wide-gap semiconductors (using the example
983 of silicon carbide), Semiconductors, 36 (2002) 1270-1275.
984 [6] L. Liu, A. Liu, S. Bai, L. Lv, P. Jin, X. Ouyang, Radiation Resistance of Silicon Carbide
985 Schottky Diode Detectors in D-T Fusion Neutron Detection, Scientific Reports, 7 (2017)
986 13376.
987 [7] L. Hrubčín, Y.B. Gurov, B. Zaťko, O.M. Ivanov, S.V. Mitrofanov, S.V. Rozov, V.G.
988 Sandukovsky, V.A. Semin, V.A. Skuratov, A Study of the Radiation Hardness of Si and SiC
989 Detectors Using a Xe Ion Beam, Instruments and Experimental Techniques, 61 (2018) 769-
990 771.

Journal Pre-proof

991 [8] G. Bertuccio, R. Casiraghi, F. Nava, Epitaxial Silicon Carbide for X-ray Detection, IEEE
992 Transactions on Nuclear Science, 48 (2001) 232-233.
993 [9] G. Bertuccio, S. Caccia, D. Puglisi, D. Macera, Advances in Silicon Carbide X-ray
994 Detectors, Nuclear Instruments and Methods in Physics Research A, 652, (2011) 193-196.
995 [10] J.E. Lees, D.J. Bassford, G.W. Fraser, A.B. Horsfall, K.V. Vassilevski, N.G. Wright, A.
996 Owens, Semi-transparent SiC Schottky diodes for X-ray spectroscopy, Nuclear Instruments
997 and Methods A, 578, (2007) 226-234.
998 [11] A.M. Barnett, Wide Band Gap Compound Semiconductor Detectors for X-ray
999 Spectroscopy in Harsh Environments, PhD Thesis, University of Leicester, Department of
1000 Physics and Astronomy, 2011.
1001 [12] G. Lioliou, H.K. Chan, T. Gohil, K.V. Vassilevski, N.G. Wright, A.B. Horsfall, A.M.
1002 Barnett, 4H-SiC Schottky Diode Arrays for X-ray Detection, Nuclear Instruments and
1003 Methods in Physics Research A, 840 (2016) 145-152.
1004 [13] G. Lioliou, N.R. Gemmell, M. Mazzillo, A. Sciuto, A.M. Barnett, 4H-SiC Schottky
1005 diodes with Ni_2Si contacts for X-ray detection, Nuclear Instruments and Methods in Physics
1006 Research A, 940 (2019) 328-336.
1007 [14] S. Zhao, G. Lioliou, A.M. Barnett, Temperature dependence of commercial 4H-SiC UV
1008 Schottky photodiodes for X-ray detection and spectroscopy, Nuclear Instruments and
1009 Methods in Physics Research A, 859 (2017) 76-82.
1010 [15] C.S. Bodie, G. Lioliou, A.M. Barnett, Hard X-ray and γ-ray spectroscopy at high
1011 temperatures using a COTS SiC photodiode, Nuclear Instruments and Methods in Physics
1012 Research A, 985 (2021) 164663.
1013 [16] S.M. Sze, K.K. Ng, Physics of Semiconductor Devices, 3rd ed., John Wiley & Sons,
1014 New Jersey, 2007.
1015 [17] H.B. Michaelson, Relation between an Atomic Electronegativity Scale and the Work
1016 Function, IBM Journal of Research and Development, 22 (1978) 72-80.
1017 [18] J.A. Kittl, M.A. Pawlak, A. Lauwers, C. Demeurisse, K. Opsomer, K.G. Anil,
1018 C. Vrancken, M.J.H. van Dal, A. Veloso, S. Kubicek, P. Absil, K. Maex, S. Biesemans, Work
1019 function of Ni Silicide Phases on HfSiON and SiO_2: NiSi, Ni_2Si, $Ni_{31}Si_{12}$, and Ni_3Si fully
1020 Silicided Gates, IEEE Electron Device Letters, 27 (2006) 34-36.
1021 [19] H.B. Michaelson, The work function of the elements and its periodicity, Journal of
1022 Applied Physics, 48 (1977) 4729-4733.
1023 [20] R. Rupp, R. Elpelt, R. Gerlach, R. Schömer, M. Draghici, A new SiC diode with
1024 significantly reduced threshold voltage, 2017 29th International Symposium on Power
1025 Semiconductor Devices and IC's (ISPSD) (2017) 355-358.
1026 [21] A.B. Renz, V.A. Shah, O. Vavasour, Y. Bonyadi, G. Baker, F. Li, T. Dai, M. Walker,
1027 P.A. Mawby, P.M. Gammon, Surface effects of passivation within Mo/4H-SiC Schottky
1028 diodes through MOS analysis, Materials Science Forum, 963 (2019) 511-515.
1029 [22] A.B. Renz, V.A. Shah, O.J. Vavasour, Y. Bonyadi, F. Li, T. Dai, G.W.C. Baker, S.
1030 Hindmarsh, Y. Han, M. Walker, Y. Sharma, Y. Liu, B. Raghothamachar, M. Dudley, P.A.
1031 Mawby, P.M. Gammon, The improvement of Mo/4H-SiC Schottky diodes via a P_2O_5 surface
1032 passivation treatment, Journal of Applied Physics, 127 (2020) 025704.

Journal Pre-proof

Journal Pre-proof

1033 [23] G. Bertuccio, P. Rehak, D. Xi, A Novel Charge Sensitive Preamplifier without the
1034 Feedback Resistor, Nuclear Instruments and Methods in Physics Research A, 326 (1993) 71-
1035 76.
1036 [24] U. Schötzig, Half-Life and X-ray Emission Probabilities of ^{55}Fe, Applied Radiation and
1037 Isotopes, 53 (2000) 469-472.
1038 [25] H. Xiaolong, Y. Shenggui, D. Chunsheng, Evaluation of the decay data of ^{109}Cd,
1039 Nuclear Instruments and Methods in Physics Research A, 621 (2010) 443-446.
1040 [26] H.R. Verma, Measurements of M and L X-ray energies and relative intensities
1041 emanating from ^{241}Am source, Applied Radiation and Isotopes, 122 (2017) 41-46.
1042 [27] M.-M. Bé, V. Chiste, C. Dulieu, X. Mougeot, E. Browne, V. Chechev, N. Kuzmenko, F.
1043 Kondev, A. Luca, M. Galan, A.L. Nichols, A. Arinc, X. Huang, Table of Radionuclides
1044 (A=22 to A=244) Bureau International des Poids et Mesures, Sèvres, 2010.
1045 [28] W. Shockley, Currents to conductors induced by a moving point charge, Journal of
1046 Applied Physics, 9 (1938) 635-636.
1047 [29] S. Ramo, Currents induced by electron motion, Proceedings of the IRE, 27 (1939) 584-
1048 585.
1049 [30] J.H. Hubbell, Review of photon interaction cross section data in the medical and
1050 biological context, Physics in Medicine and Biology, 44 (1999) R1-R22.
1051 [31] J.H. Hubbell, S.M. Seltzer, Tables of X-Ray Mass Attenuation Coefficients and Mass
1052 Energy-Absorption Coefficients (Version 1.4), National Institute of Standards and
1053 Technology, Gaithersburg, 2004.
1054 [32] P.M. Gammon, A. Pérez-Tomás, V.A. Shah, O. Vavasour, E. Donchev, J.S. Pang, M.
1055 Myronov, C.A. Fisher, M.R. Jennings, D.R. Leadley, P.A. Mawby, Modelling the
1056 inhomogeneous SiC Schottky interface, Journal of Applied Physics, 114 (2013) 223704.
1057 [33] F. Roccaforte, G. Brezeanu, P.M. Gammon, F. Giannazzo, S. Rascunà, M. Saggio,
1058 Schottky Contacts to Silicon Carbide: Physics, Technology and Applications, in Advancing
1059 Silicon Carbide Electronics Technology I, Materials Research Forum LLC, Millersville,
1060 2018.
1061 [34] M. Mazzillo, A. Sciuto, G. Catania, F. Roccaforte, V. Raineri, Temperature and Light
1062 Induced Effects on the Capacitance of 4H-SiC Schottky Photodiodes, IEEE Sensors
1063 Journal, 12 (2012) 1127-1130.
1064 [35] G. Lioliou, G., A.M. Barnett, Electronic Noise in Charge Sensitive Preamplifiers for
1065 X-ray Spectroscopy and the Benefits of a SiC Input JFET, Nuclear Instruments and Methods
1066 in Physics Research A, 801 (2015) 63-72.
1067 [36] G. Bertuccio, A. Pullia, G. De Geronimo, Criteria of Choice of the Front-End Transistor
1068 for Low-Noise Preamplification of Detector Signals at Sub-Microsecond Shaping Times for
1069 X- and γ-ray Spectroscopy, Nuclear Instruments and Methods in Physics Research A, 380
1070 (1996) 301-307.
1071 [37] G. Bertuccio, A. and Pullia, A Method for the Determination of the Noise Parameters in
1072 Preamplifying Systems for Semiconductor Radiation Detectors, Review of Scientific
1073 Instruments, 64, (1993) 3294-3298.
1074 [38] G. Bertuccio, R. Casiraghi, Study of Silicon Carbide for X-ray Detection and
1075 Spectroscopy, IEEE Transactions on Nuclear Science, 50 (2003) 175-185.

Journal Pre-proof

1076 [39] R.H. Pehl, F.S. Goulding, D.A. Landis, M. Lenzlinger, Accurate determination of the
1077 ionization energy in semiconductor detectors, Nuclear Instruments and Methods, 59 (1968)
1078 45-55.
1079 [40] G. Bertuccio, D. Maiocchi, Electron-Hole Pair Generation Energy in Gallium Arsenide by
1080 x and γ Photons, Journal of Applied Physics, 92 (2002) 1248-1255.
1081 [41] A. Owens, Semiconductor Radiation Detectors, CRC Press, Boca Raton, 2019.
1082 [42] M.D.C. Whitaker, G. Lioliou, A.B. Krysa, A.M. Barnett, $Al_{0.6}Ga_{0.4}As$ X-ray avalanche
1083 photodiodes for spectroscopy, Semiconductor Science and Technology, 35 (2020) 095026.
1084 [43] A.D.T. Short, An Evaluation of Gallium Arsenide for Detector Applications in X-ray
1085 Astronomy, PhD Thesis, Department of Physics and Astronomy, University of Leicester,
1086 Leicester, UK, 1997.
1087 [44] O. Maslyanchuk, M. Solovan, V. Brus, P. Maryanchuk, E. Maistruk, I. Fodchuk, V.
1088 Gnatyuk, Charge transport features of CdTe-based X- and γ-ray detectors with Ti and TiO_x
1089 Schottky contacts, Nuclear Instruments and Methods in Physics Research A, 988 (2021)
1090 163920.
1091 [45] V. Gnatyuk, O. Maslyanchuk, M. Solovan, V. Brus, T. Aoki, CdTe X/γ-ray detectors
1092 with different contact materials, Sensors, 21 (2021) 3518.

Journal Pre-proof

G. Lioliou: Methodology, Validation, Formal analysis, Investigation, Data Curation, Writing - original draft, Writing - Review & Editing, Visualization. **A.B. Renz**: Methodology, Validation, Investigation, Data Curation. **V.A. Shah:** Conceptualization, Investigation, Resources, Data Curation, Writing - Review & Editing, Supervision, Project administration, Funding acquisition. **P.M. Gammon**: Conceptualization, Investigation, Resources, Data Curation, Writing - Review & Editing, Supervision, Project administration, Funding acquisition. **A.M. Barnett**: Conceptualization, Methodology, Validation, Formal analysis, Investigation, Resources, Data Curation, Writing - Original Draft, Writing - Review & Editing, Visualization, Supervision, Project administration, Funding acquisition.

Journal Pre-proof

Journal Pre-proof

Declaration of interests

☒ The authors declare that they have no known competing financial interests or personal relationships that could have appeared to influence the work reported in this paper.

☐The authors declare the following financial interests/personal relationships which may be considered as potential competing interests:

Journal Pre-proof